Plasmonic Control of Radiative Properties of Semiconductor Quantum Dots Coupled to Plasmonic Ring Cavities

Aliaksandra Rakovich, Pablo Albella, Stefan A. Maier.

EXSS group, Physics Department, Imperial College London, UK.

SUPPLEMENTARY INFORMATION

Fabrication of plasmonic ring cavities

Plasmonic Ring Cavity (PRC) structures were fabricated using standard e-beam lithography (EBL) technique. Poly(methyl methacrylate) (PMMA) was used as a positive resist for EBL exposure to define a mask for deposition of 40 nm of gold (Au). 950PMMA in anisole (A4) was bought from MicroChem and used as received. After metal deposition, PMMA mask was lifted off for 2-3 days in acetone. Remaining Au structures were imaged using Scanning Electron Microscopy (SEM). Figure S1-1 shows some SEM images of the fabricated PRC structures of varying diameters and thicknesses. Dimensions of these structures are summarized in Table S1.

Non-Concentric Ring-Disk Cavities were fabricated in similar fashion, with the disk and the ring being deposited in either the same EBL step, or in separate steps with alignment of the two

layers. The latter method produced more uniform rings and allowed smaller ring-disk separations. Some of the representative SEM images of NCRDCs are shown in Figure S1-2. Figure S2 shows the intensity enhancements maps for these NCRDCs 10 nm above the substrate, obtained using FDTD method.

Quantum dots (QDs) – sourcing and spectral properties

Carboxyl acid-functionalized CdSe/ZnS QDs were purchased from Molecular Probes (Invitrogen, Catalog no. Q21311MP) and used as received. Their absorption and photoluminescence spectra were recorded for confirmation purposes; these are shown in Figure S3A. Time-resolved fluorescence decay curves of these QDs before and after conjugation to quartz were also recorded and found to be similar (Figure S3B). Only a small change was observed and this can be attributed to the different surface chemistry of the conjugated QDs.

Attachment of QDs via 2-step EBL

Sample with PRC structures was covered with ~220 nm of PMMA by spin-coating and this PMMA layer was exposed using EBL. This EBL write was aligned to the markers of the previous layer (that included the PRC structures), so that ring shaped gaps were opened in the PMMA layer, aligned to the inside of the PRCs (Figure S4). The radius of the ring gaps was increased every 5-6 columns of the PRC arrays, thus reducing the distance from the inner PRC walls to the opened gaps (see Figure S5). As a result, the distance between the inner PRC wall and ring of QDs also decreased, once QDs were attached to the substrate in these opened gaps. Thus the radius of the ring defined by this second EBL step was termed R_{QD} (Figure S5i).

In order to evaluate the change of QDs' radiative behavior due to the coupling to PRC structures, measurements were performed on rings of QDs in the presence and absence of PRC (standalone QD rings). The main text (Figure 5) shows the results of these measurements. Here we add the non-normalised data (Figure S6).

Theoretical Calculations of Dark field spectra of PRCs and NCRCs

Dark field spectra of PRCs and NCRDCs (with 1nm Cr underneath) and supported on silica substrate were calculated numerically using commercially available finite element methods (Lumerical FDTD and COMSOL Multiphysics 4.3). The PRCs were modeled by subtracting two concentric gold disks of radius r1 and r2, and then placed inside a tetrahedral simulation space surrounded by perfectly matched layers (PMLs) and scattering boundary conditions to absorb scattered light. The refractive index of gold, chromium and silica were taken from Palik.[1]

The scatterers (PRCs and NCRCs in our case) were excited using an unpolarized plane wave incident at an angle of 60deg with respect to the normal of the substrate. To simulate the dark field scattering under unpolarized plane wave excitation, two simulations with orthogonal polarizations (E_s and E_p) were performed. Scattering results were calculated by incoherently summing the results from these two polarized simulations according to:

$$<|E|^2>=1/2\bullet|E_s|^2+1/2\bullet|E_p|^2 \qquad \text{(S1)}$$

The collection angle associated with a given numerical aperture was included in the simulation by integrating the far-field scattering only over the boundary of a spherical cap with an opening half angle of $sin^{-1}(NA)/n_{env}$ being NA=0.8 the numerical aperture of our objective and n_{env} the

refractive index of the environment (air in our case). More complex factors arising from the use of high numerical aperture objectives such as apodization effects, were neglected, and may be the origin of the small discrepancies between experimental and numerical dark field results.

Averaging of theoretical decay rates to compare with experimental data

The decay rate of a dipole, when coupled to a specific PRC, was calculated theoretically for several wavelengths, and for a range of distances from the PRC's centre. These data were then used to obtain averaged theoretical decay rate enhancement factors for different radii of QDs' rings (or equivalently, QD-PRC separations). The averaging procedure took into account two factors: the number of QDs (dipoles) contributing to the measured signal at a particular distance from the centre of the PRC structure, and the spectral width of QDs' emission.

Since the area where QDs were deposited was defined lithographically, every QDs' ring had a specific width associated with it. For example, for ring of radius of 100 nm, it is expected that QDs were deposited in a band 30 nm wide (i.e. extending from 85 to 115 nm from PRCs' centre). However, the number of QDs that can be found at these distances are different, and has $\sim 2\pi R$ dependence. Therefore, for both X and Y directions and for every wavelength, the initial results were number-averaged to account for this dependency:

$$\bar{\gamma}_{xy}(\lambda) = \frac{1}{2}\left(\frac{\sum_{i=d_i}^{i=d_f} n_{ix}\gamma_{ix}(\lambda)}{\sum_{i=d_i}^{i=d_f} n_{ix}} + \frac{\sum_{i=d_i}^{i=d_f} n_{iy}\gamma_{iy}(\lambda)}{\sum_{i=d_i}^{i=d_f} n_{iy}}\right) \quad \text{(S2)}$$

These results were then averaged spectrally to account for the width of QDs' emission spectrum. This was achieved by using the values of relative emission intensity of QDs at each wavelength as weighing coefficients (see Figure S7 for diagrammatic explanation):

$$\bar{\gamma}_{xy,\lambda} = \frac{\sum_{i=\lambda_i}^{i=\lambda_f} k_i * \bar{\gamma}_{xy}(\lambda)}{\sum_{i=\lambda_i}^{i=\lambda_f} k_i} \quad \text{(S3)}$$

Differences between theoretical and experimental spectra of NCRDCs

During characterization of the NCRDCs, it was observed that experimentally-measured dark-field spectra deviated from theoretically calculated scattering spectra. Most of these deviations can be attributed to imperfect geometry of the fabricated structures.

Firstly, both the disk and the ring edges have imperfections, so their lateral dimensions (thickness, radius, *etc*.) are not uniform. As a result, the quality of the resonances is not ideally, resulting in broadening of the plasmonic peaks. Furthermore, the gap between the disk and the ring in NCRDCs is also not uniform resulting in reduced coupling between disk and ring. From FDTD calculations, we find that the overall effect of this is decreased scattering from lower order modes (higher wavelengths) and slight blue-shift of the peaks. Finally, the ellipticity of the disk along the Y-direction strengthens the resonances that have a dipole-like resonance between the disk and the ring along the diagonals, for example does resonance *ii* in figure 8D of the main paper. In fact, this is the main reason why experimentally we mainly see scattering at 650 nm.

Charge distribution calculations

Charge distribution maps shown in Figures 2 and 8 of the main manuscript were obtained by calculating the divergence of the electric field using FDTD methods. Electric field distributions were calculated on the upper surface of the structure, at two very closely spaced planes. The mesh step in the Z-direction was chosen such as to ensure occurrence of at least 5 mesh points

between these two planes, since divergence is extremely sensitive to discretization used.[2] Divergence was then approximated to be the difference between the electric field values along the two planes. To obtain charge oscillation movies, the phase of the divergence was continuously varied from 0 to 2π. These movies are included as additional material.

Size of hotspots comparison

The theoretical size of the hotspots was compared for a NCRDC and a dimer disk nanoantenna (DDNA) resonant at 650 nm. The NCRDC chosen was one where resonance at 650 nm was confirmed experimentally, and it consisted of 40 nm high Au D350t45 PRC and a 90 nm disk placed 15 nm away from the inner wall of the PRC. DDNA structure consisted of two Au disks, 40 nm high and 90 nm in diameter, separated by 15 nm. FDTD calculations were used to simulate the response of these structures at 650 nm incident plane wave; particular attention was paid to the field enhancement in the gaps of the structures in XY and YZ directions. Cross-sections were taken from the E/E0 maps (see Figure S8), and FWHMs of these were then extracted from cross-sections; the values of the FWHMs are summarized in Table S2. The ratio of the hotspots was estimated assuming roughly a spheroidal shape for comparison purposes:

$$\frac{V_{NCRDC}}{V_{DDNA}} \cong \frac{\left(D_x * D_y * D_z\right)_{NCRDC}}{\left(D_x * D_y * D_z\right)_{DDNA}} \approx \mathbf{3} \tag{S4}$$

FIGURES.

Figure S1-1.

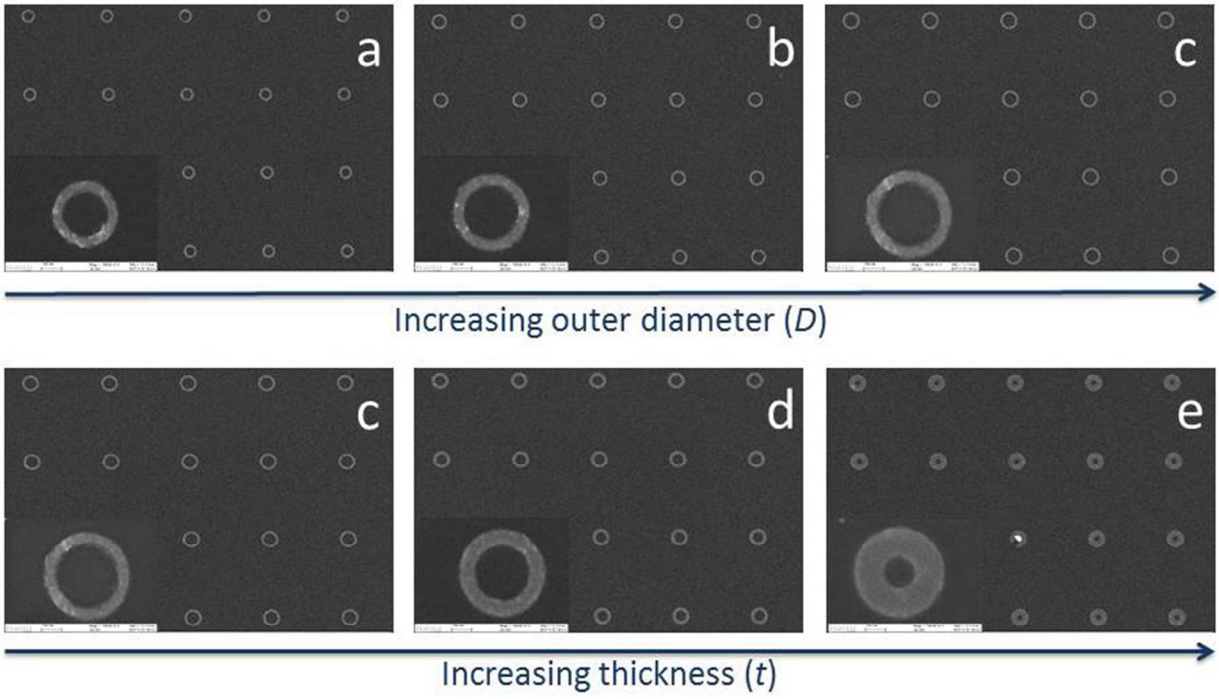

Figure S1-1. SEM images of Plasmonic Ring Cavities. The top row shows structures with similar ring thicknesses (average t~55 nm) but increasing diameters (325 to 440 nm left to right). The bottom row shows PRCs with similar diameters (~440 nm) but increasing wall thicknesses (60 to 140 nm).

Figure S1-2.

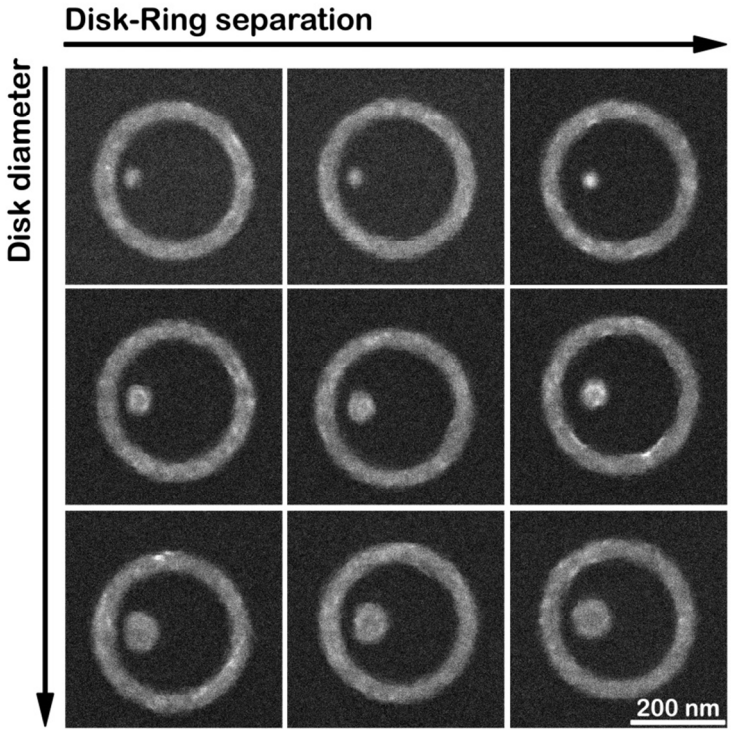

Figure S1-2. SEM images of Non-Concentric Ring-Disk Cavities. For all NCRDCs, the rings had diameters of ~350 nm and thickness of ~45 nm. NCRDCs with three different disk diameters were fabricated: ~30, 60 and 90 nm (top to bottom row). Note that diameters indicated here are along the X-direction (the symmetry axes). Some of the disks were found to have larger diameters along the Y-direction. The separation between the disk and the ring was also varied (increases left to right).

Figure S2

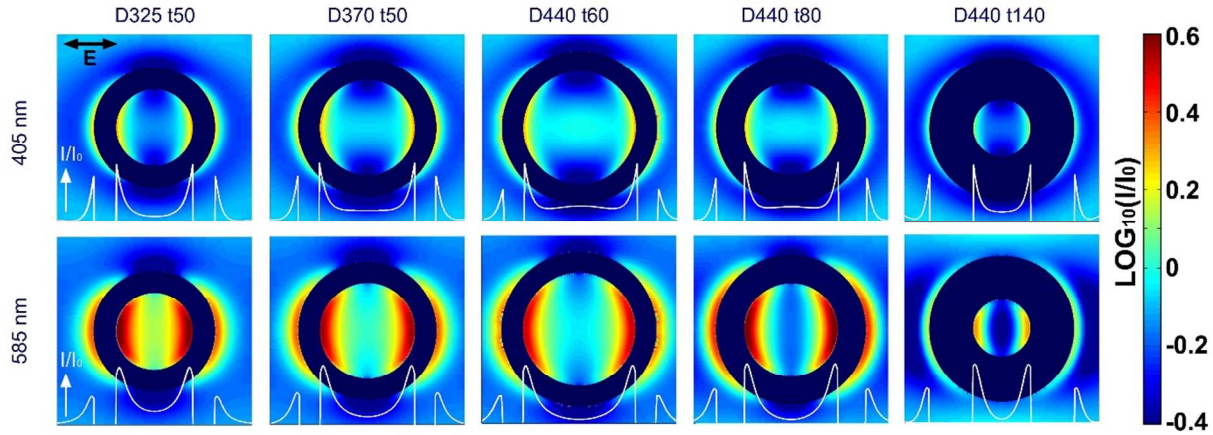

Figure S2. Intensity enhancement maps for 40 nm high Au PRCs of different dimensions, on a 1 nm Cr adhesion layer, on quartz substrate and at normal incidence. Maps were calculated using the FDTD method at a height of 10 nm above the substrate for two wavelengths: excitation wavelengths used (top row) and QDs' emission wavelength (bottom row). The white lines in the maps shown cross sectional values of intensity enhancement through the centers of the PRCs.

Figure S3

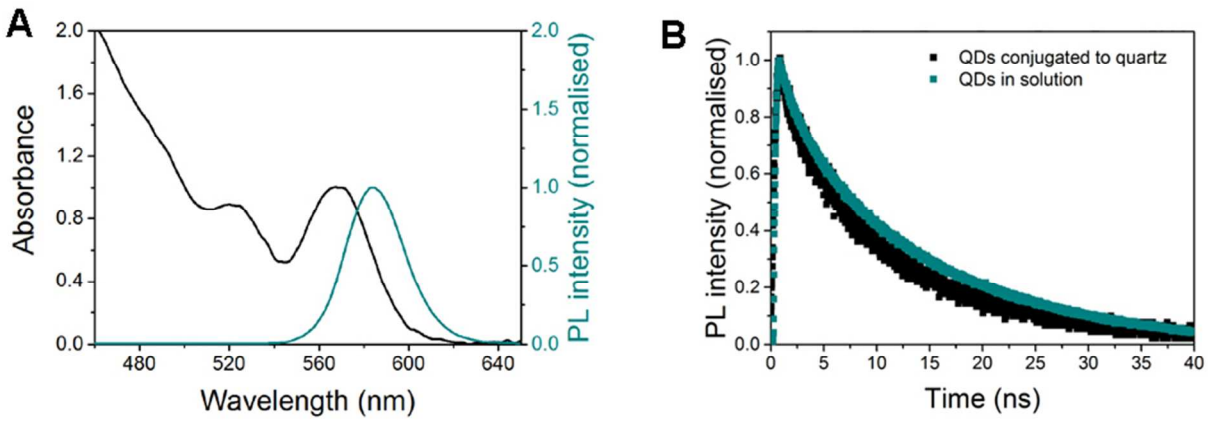

Figure S3. Optical properties of CdSe/ZnS QDs showing (A) absorption (black line) and photoluminescence spectra (cyan line) of stock QDs dissolved in water and (B) time-resolved fluorescence decay of these QDs in aqueous solution (cyan scatter points) and when conjugated to a quartz substrate (black scatter points).

Figure S4

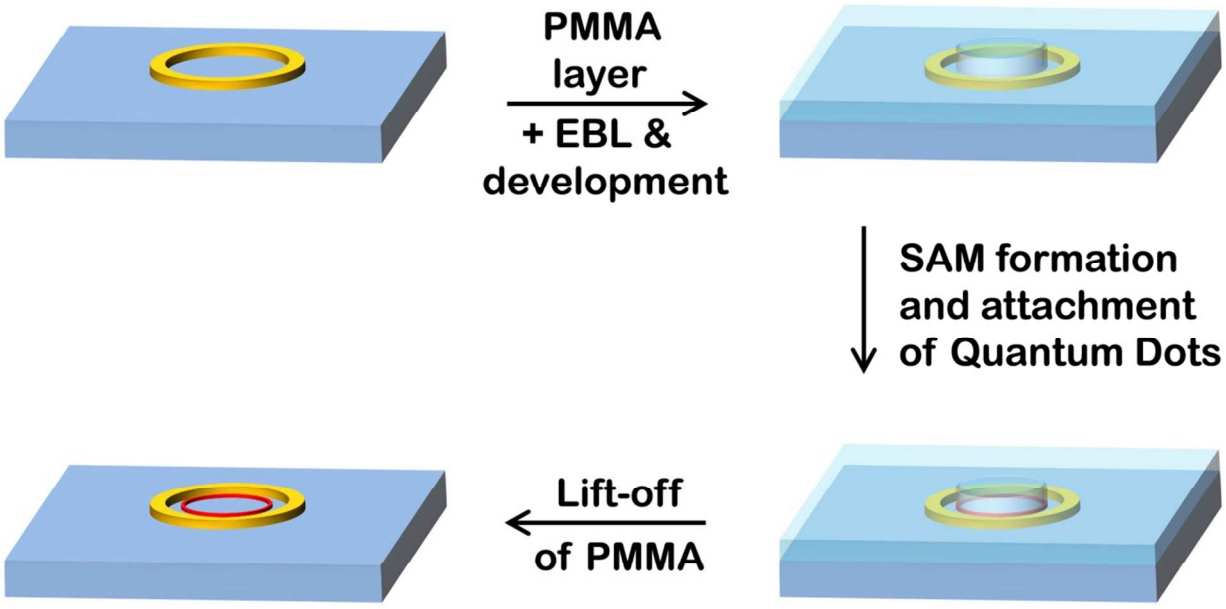

Figure S4. Scheme depicting fabrication steps to achieve localized attachment of colloidal QDs to the quartz substrate inside PRCs. Fabrication involved: defining the area of attachment using e-beam exposure of PMMA mask; formation of self-assembled monolayer on the exposed substrate surface and chemical conjugation of QDs to this monolayer; and the lift-off of the PMMA mask. Dimensions are not to scale.

Figure S4

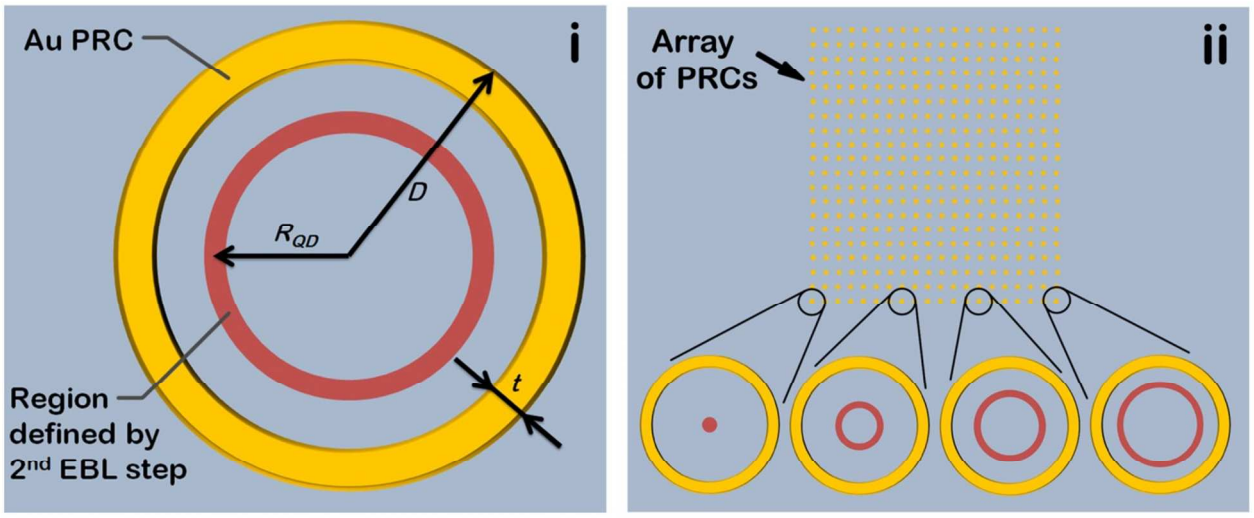

Figure S5. Schematic representation of the geometries of QDs and PRCs. (i) shows a single gold PRC of diameter *D* and thickness *t*. Also shown is a representative region where QDs were attached, as defined by the second EBL step. R_{QD} is defined as the distances from the centre of the PRC to the middle of the attachment region. (ii) shows an array of PRCs and a diagrammatic representation of QDs attached inside PRCs – as R_{QD} was increased (every 5-6 columns), the distance from inner PRC wall to QDs decreased.

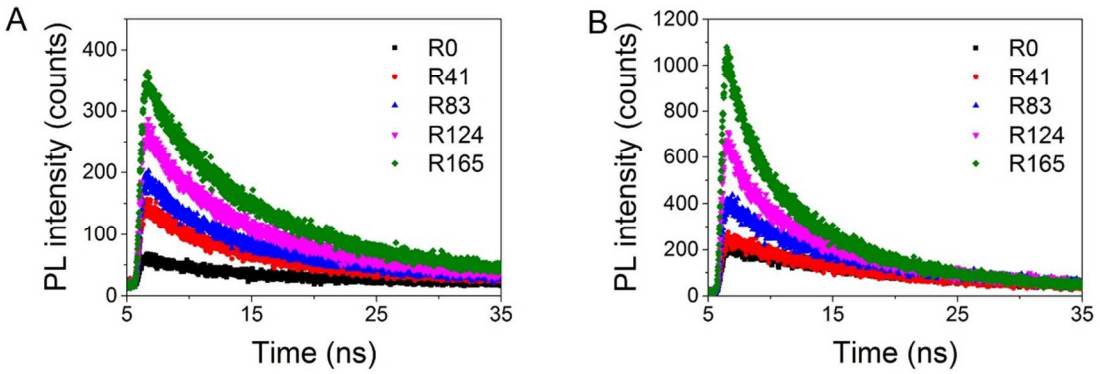

Figure S6. Non-normalized lifetime data for rings of QDs of increasing radii (R_{QD}, given in the data labels) (A) standalone on quartz substrate and (B) placed central inside a D440t60 PRC.

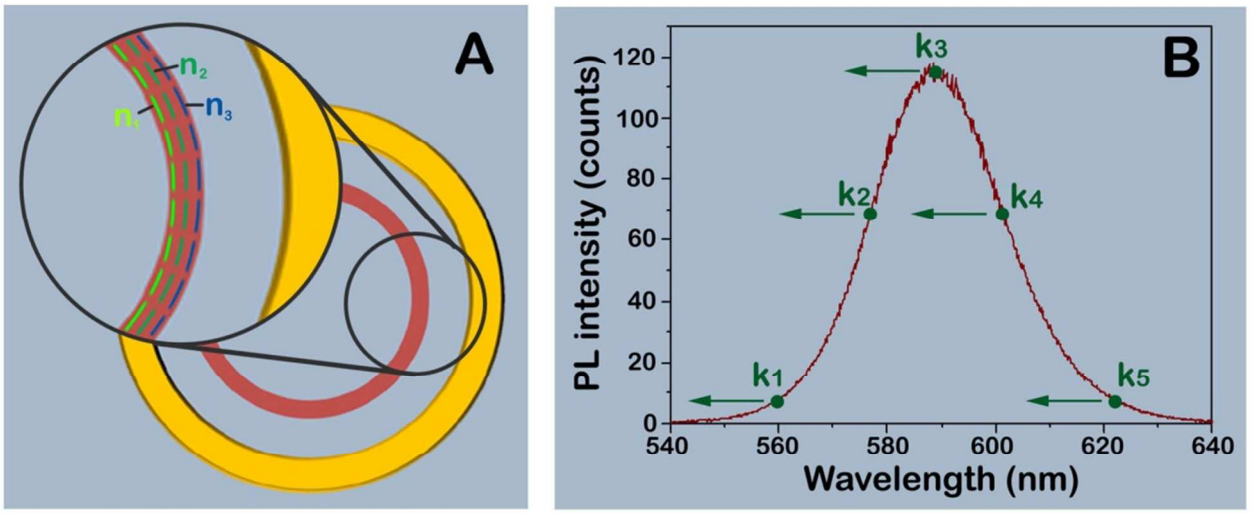

Figure S7. Averaging of theoretical decay rates. For comparison with experimental data, theoretical decay rates were averaged over QDs' position (A) and over QDs' emission spectrum (B). For position-averaging, the weighting coefficients were the relative number of QDs (n_i) at different distances from ring centre, indicated by dashed lines in (A). These positionally-averaged theoretical decay rates were then used to determine the final average of decay rate enhancement, using QDs' emission spectrum as the weighing coefficients in equation S3 (k_i's, as defined in B).

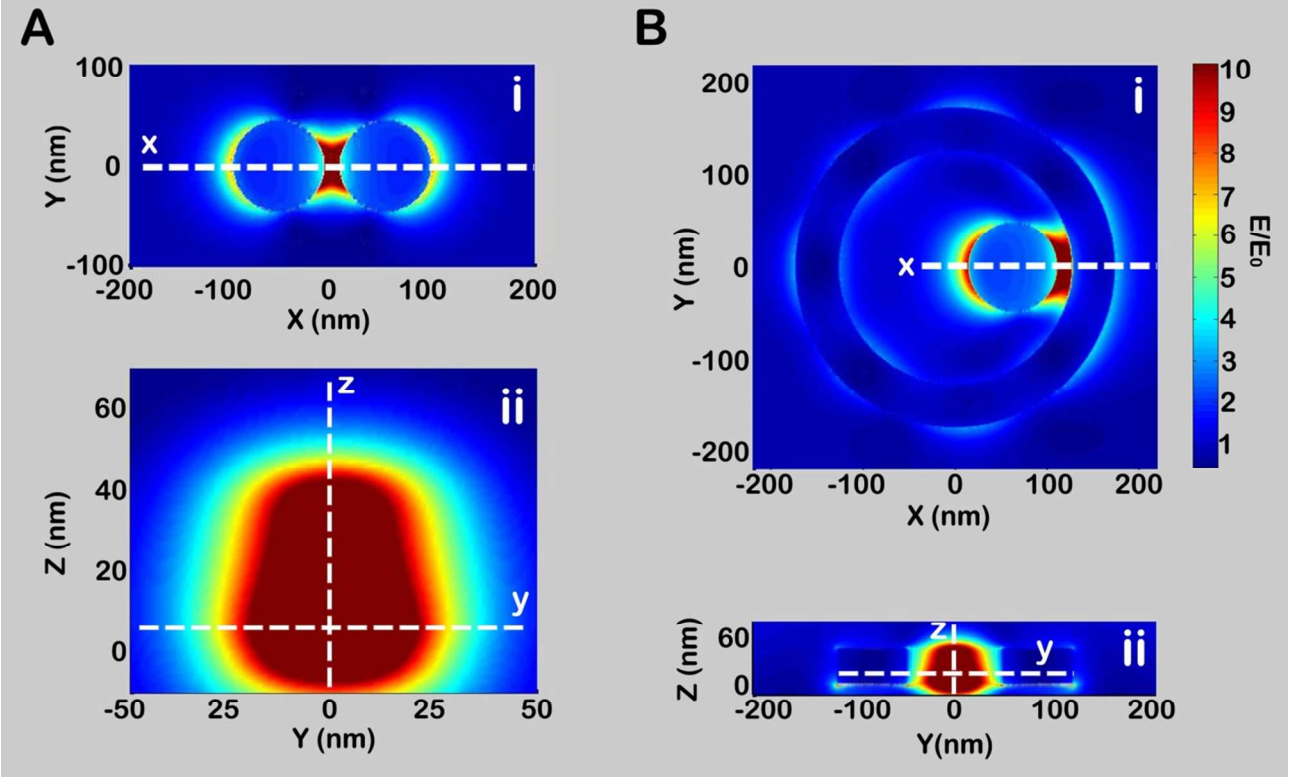

Figure S8. Comparison of hotspots for Disk-Dimer NanoAntenna (A) and Non-Concentric Ring-Disk Cavity (B) with same material composition, structure height, gap size and resonance position (650 nm). Cross-sections of the (i) XY and (ii) YZ maps were used to extract FWHM values in the x, and y and z direction respectively. The ratio of the multiple of these three showed that NCRDCs have hotspots approximately 3 times bigger than DDNAs. The PRC was composed from D350t45 PRC and a disk of 90 nm diameter. The DDNA also had both disks of 90 nm diameter. Both NCRDCs and DDNA had a gap of 20 nm and were 40 nm high (Au on quartz substrate).

TABLES.

Table S1. Dimensions of PRCs shown in Figure S1. The properties of these PRCs are discussed in the main paper, referred to by the labels given in the first column.

Label in Figure S1 / Label in main text	*Outer Diameter D (nm)*	*Inner Diameter Di (nm)*	*Wall thickness t (nm)*
a / D330t50	324 ± 6	230 ± 3	47 ± 4
b / D370t50	367 ± 18	275 ± 4	46 ± 11
c / D440t60	442 ± 8	326 ± 4	58 ± 6
d / D440t80	439 ± 13	281 ± 5	79 ± 6
e / D440t140	442 ± 4	162 ± 3	140 ± 4

Table S2. Approximate FWHMs of the E/E0 cross-sections for DDNA and NCRDC structures resonating at 650 nm.

Structure	*Dx (nm)*	*Dy (nm)*	*Dz (nm)* *
DDNA	16.2	19.2	42.5
NCRDC	15.9	58.4	42.7

* Only positive Z values were considered (i.e. above substrate)

Supplementary References:

(1) Edward D. Palik. *Handbook of Optical Constants of Solids*; Elsevier, 1997; pp. 5–114.

(2) Kottmann, J. P.; Martin, O. J. F.; Smith, D. R.; Schultz, S. Field Polarization and Polarization Charge Distributions in Plasmon Resonant Nanoparticles. *New J. Phys.* **2000**, *2*, 27.1–27.9.